



Continuation of long-term global SO₂ pollution monitoring from OMI to OMPS

Yan Zhang^{1,2}, Can Li^{1,2}, Nickolay A. Krotkov², Joanna Joiner²

¹Earth System Science Interdisciplinary Center, University of Maryland, College Park, MD 20742, USA

5 ²NASA Goddard Space Flight Center, Greenbelt, MD 20771, USA

Correspondence to: Yan Zhang (yan.zhang@nasa.gov)

Abstract. Over the past 20 years, advances in satellite remote sensing of pollution-relevant species have made space-borne observations an increasingly important part of atmospheric chemistry research and air quality management. This progress has been facilitated by advanced UV-Vis spectrometers, such as the Ozone Monitoring Instrument (OMI) on board the
10 NASA EOS Aura satellite, and continues with new instruments, such as the Ozone Mapping and Profiler Suite (OMPS) on board the NASA-NOAA Suomi National Polar-orbiting Partnership (SNPP) satellite. In this study, we demonstrate that it is possible, using our state-of-the-art principal component analysis (PCA) retrieval technique, to continue the long-term global SO₂ pollution monitoring started by OMI with the current and future OMPS instruments that will fly on the NOAA Joint Polar Satellite System (JPSS)-1, -2, -3, -4 satellites in addition to SNPP, with a very good consistency of retrievals from
15 these instruments. Since OMI SO₂ data have been primarily used for 1) providing regional context on air pollution and long-range transport on a daily basis; and 2) providing information on point emission sources on an annual basis after data averaging, we focused on these two aspects in our OMI-OMPS comparison. Four years of retrievals during 2012-2015 have been compared for three regions: eastern China, Mexico, and South Africa. In general, the comparisons show high temporal correlations ($r = 0.79-0.96$) of SO₂ mass between the two instruments and near unity regression slopes (0.76-0.97). The
20 annual averaged SO₂ loading difference between OMI and OMPS is small (< 0.03 Dobson Unit (DU)) over South Africa and up to 0.1 DU over eastern China). We also found a very good correlation ($r=0.92-0.97$) in the spatial distribution of annual mean SO₂ between OMI and OMPS over the three regions during 2012-2015. For 82% of the days, the two instruments have a spatial correlation coefficient of 0.6 or better over the Mexico region. It is worth noting that such consistent retrievals were achieved without any explicit adjustment to OMI or OMPS radiance data, and that the retrieval agreement may be further
25 improved by introducing a more comprehensive Jacobian lookup table than currently used.

1 Introduction

Sulfur dioxide (SO₂) is an important pollutant gas that has significant impacts on the environment and climate at global, regional, and local scales. It oxidizes to form sulfate aerosols that reduce visibility, affect cloud formation, and lead
30 to acid deposition. Anthropogenic sources of SO₂, consisting primarily of fossil fuel burning (Fioletov et al., 2015; Li et al., 2010a, 2010b)(Fioletov et al., 2015; Li et al., 2010b), metal smelting (Carn et al., 2007), and oil and gas refining (McLinden



et al., 2014), contribute roughly 70% of global SO₂ emissions (Smith et al., 2011). The remainder of SO₂ emissions is from natural sources, e.g. volcanic eruptions and degassing, and sea spray (Faloona et al., 2010).

Satellite remote sensing using spectral fitting techniques in the ultraviolet (UV) has been employed for global retrievals of SO₂ total columns (e.g., Eisinger and Burrows, 1998; Fioletov et al., 2013; Krotkov et al., 2010, 2016; Li et al., 2013). Space-based SO₂ retrievals were first demonstrated for the El Chichon volcanic eruption using the Total Ozone Mapping Spectrometer (TOMS) (Krueger, 1983). Since then, satellite retrievals of global SO₂ pollution have undergone substantial improvements. Measurements of anthropogenic SO₂ have been demonstrated using several hyperspectral UV spectrometers such as the Global Ozone Monitoring Experiment (GOME) (e.g., Eisinger and Burrows, 1998), GOME-2 (e.g., Nowlan et al., 2011), SCanning Imaging Absorption SpectroMeter for Atmospheric CHartographY (SCIAMACHY) (e.g., Lee et al., 2009), Ozone Monitoring Instrument (OMI) (Fioletov et al., 2015; Krotkov et al., 2006, 2008, 2016; Li et al., 2010a, 2010b; McLinden et al., 2014, 2016a), and the nadir mapper of the Ozone Mapping and Profiler Suite (OMPS) (Yang et al., 2013). However, it is challenging to build consistent, multi-satellite datasets necessary for long-term monitoring, as different characteristics between satellite instruments must be accounted for; relatively small inconsistencies in satellite radiance measurements and calibration may introduce large retrieval biases. Previous studies also suggested that the spatial resolution of a satellite instrument is the main limiting factor in detection of SO₂ emissions from point sources (Fioletov et al., 2013, 2015). This causes additional measurement differences in SO₂ loading from different instruments. Stitching together satellite SO₂ retrievals from different instruments and processed with various algorithms therefore usually requires empirical bias corrections (Fioletov et al., 2013).

Recently, a principal component analysis (PCA) algorithm was developed and applied to OMI (Li et al., 2013, 2016). This approach greatly reduces the noise and bias compared to the previous band residual difference (BRD) OMI SO₂ algorithm (Krotkov et al., 2006), and allows smaller sources to be detected from space (Fioletov et al., 2015, (McLinden et al., 2016b)) and trends to be studied for more regions. One of the strengths of the PCA technique is that it doesn't require instrument-specific, explicit corrections to satellite-measured radiance data. This makes it relatively straightforward to adapt to other instruments and reduces the chance of introducing retrieval biases between different instruments. In this paper we apply the PCA technique to the OMPS measurements (2012-2015) to examine the feasibility of continuing the OMI anthropogenic SO₂ dataset with OMPS.

2 OMI and OMPS SO₂ data

2.1 OMI operational PCA PBL SO₂

The Ozone Monitoring Instrument (OMI) is a nadir-viewing UV/Visible spectrometer (Levelt et al., 2006b) onboard NASA's Aura satellite launched in 2004 (Schoeberl et al., 2006). It measures sunlight backscattered from the Earth and covers the wavelength range from 270 to 550 nm at approximately 0.5-0.6 nm spectral resolution. The nominal pixel size of OMI is ~13 km by 24 km at nadir and ~28 km by 150 km at the swath edges. The swath is ~2600 km wide and



contains 60 cross-track binned field-of-views (FOVs or “rows”). The current local equator crossing time is about 13:38. OMI measurements of SO₂ are one of key objectives of the OMI mission (Levelt et al., 2006a), which is aimed at advancing our understanding of pollutant sources and transformation processes and enabling the application of OMI data to inform public policy (Streets et al., 2013).

5 This study focuses on anthropogenic SO₂ that is mainly distributed within the planetary boundary layer (PBL) near source regions. Therefore we use the OMI operational PCA PBL SO₂ product (OMSO2 v1.2.0). It employs a PCA technique applied to OMI radiances between 310.5 and 340 nm to derive spectral features from the full spectral content, and uses them to represent various interfering processes in spectral fitting to reduce their impacts. This greatly reduces OMI product spatially-dependent biases as compared with the original OMI PBL SO₂ product (Krotkov et al., 2006) and decreases
10 retrieval noise by a factor of 2 (Li et al., 2013). Details of the PCA algorithm and the OMI PBL SO₂ data quality are provided in Li et al. (2013) and Krotkov et al. (2016). The product is publicly available from the NASA Goddard Earth Sciences (GES) Data and Information Services Center (DISC) (http://disc.sci.gsfc.nasa.gov/Aura/data-holdings/OMI/omso2_v003.shtml). It contains SO₂ vertical column densities (VCDs) in Dobson units (1 DU = 2.69 × 10¹⁶ molecules cm⁻²). Beginning in 2007, some cross track positions of OMI have been affected by FOV blockage and scattered
15 light (i.e., the so called the “row anomaly”). We exclude pixels with none zero values in the XTrackQualityFlag data field in the L1B data to avoid influence of row anomaly. We also exclude pixels with large FOVs at the edges of the swath (rows < 5 or > 54, zero-based).

2.2 OMPS SO₂ data

The nadir mapping component of the OMPS is a nadir-viewing UV spectrometer. The first copy has been flying on
20 board the NASA–NOAA Suomi National Polar-orbiting Partnership (SNPP) spacecraft since 2011 (Dittman et al., 2002; Flynn et al., 2014; Sefior et al., 2014). SNPP continues the long-term record of climate quality observations established by NASA’s Earth Observation System (EOS) satellites. It crosses the equator each afternoon at about 13:30 local time, ~10 minutes ahead of the OMI equator crossing time. OMPS measures backscattered UV radiance spectra from the Earth and solar irradiance in the 300–380 nm wavelength range at a spectral resolution of ~1 nm. It covers a ~2800 km cross-track
25 swath (110° FOV) with a nadir pixel size of 50 km × 50 km in the nominal observation mode. Although it has coarser spectral and spatial resolutions and expected higher detection thresholds for emissions from point sources as compared with OMI (Fioletov et al., 2013), it is still suitable for monitoring large anthropogenic SO₂ pollution (Yang et al. 2013; Krotkov et al., 2016).

Here, we apply the same PCA retrieval technique described above to OMPS in order to obtain the total SO₂ VCDs.
30 The main difference between the OMPS and OMI PCA algorithms is that for the current OMI operational product, we only retrieve SO₂ for pixels with slant column ozone, O₃ < 1500 DU, while for OMPS, we retrieve SO₂ for all pixels with solar zenith angle (SZA) < 75° in order to obtain better spatial coverage at high latitudes in winter (particularly near the edge of the swath). We have tested OMI retrievals using the same SZA threshold as OMPS, and found results to be very similar to



the operational product. Similar to the processing of OMI data, we also exclude OMPS pixels with large FOVs at the edges of the swath (rows <2 or >33 zero-based).

Another difference is that in the spectral fitting for the operational OMI product, up to 20 principal components (PCs) derived from radiance data are used. For OMPS, we use up to 15 PCs. We found that fewer PCs are required in OMPS retrievals to achieve a background bias reduction similar to that for OMI. Both OMI and OMPS algorithms employ a simplified fixed SO₂ Jacobians table, calculated assuming the same surface albedo (0.05), surface pressure (1013.25hPa), fixed solar zenith angle (30°), viewing zenith angle (0°), and O₃ and temperature profiles representative of typical mid-latitude conditions (Krotkov et al., 2008). In the future, we plan to enhance the look-up table for SO₂ Jacobians to more accurately account for different measurement conditions.

10 2.3 OMI and OMPS data filtering and gridding

In order to account for different FOV sizes, we averaged both OMI and OMPS SO₂ pixels (level 2) to the same 0.5° latitude by 0.5° longitude grid daily from 2012 to 2015. Only clear sky data, defined as pixels with effective cloud radiance fraction $< 30\%$, were used. We also excluded large negative outliers in data gridding (< -1 DU for OMI and < -0.5 for OMPS). This is due to the fact that the standard deviation of OMI retrievals is greater than that of OMPS (~ 0.5 DU for OMI vs. $\sim 0.2-0.3$ DU for OMPS) over the presumably SO₂-free equatorial Pacific. No empirical bias correction was applied to the gridded SO₂ data.

3.1 Annual/regional average SO₂

Global annual average (2012) SO₂ columns for both OMPS and OMI are presented in Fig. 1. In the South Atlantic Anomaly (SAA) region, SO₂ data are screened. In this region, Earth's magnetic field traps high-energy charged particles. These particles can cause higher-than-normal irradiance to the low orbiting satellite detector (e.g., OMI), and decrease the quality of measurements, notably in UV.

In Fig. 1, SO₂ retrievals from both OMPS and OMI are consistent. Both OMI and OMPS PCA SO₂ data show regions with major anthropogenic sources including eastern China, South Africa, Mexico, the Persian Gulf, and India, as well as a number of degassing and eruptive volcanoes (e.g., Mount Etna). For the regional comparisons, we focus on eastern China, Mexico, and South Africa. These are the regions affected by anthropogenic SO₂ pollution due to extensive emissions from coal-fired power plants and industrial processes (Krotkov et al., 2016). Mexico also has substantial volcanic SO₂ emissions from Popocatepetl volcano south of Mexico city (de Foy et al., 2009). The regions are situated in different latitude bands/climate zones and have different SO₂ loadings. This allows us to evaluate OMI and OMPS retrieval performance under a broad range of conditions. The three regions are outlined as black boxes in Fig. 1.

Figure 2 shows that both OMPS and OMI capture the details of the annual average spatial distribution of the SO₂ pollution over these regions in 2012. The average SO₂ pollution columns over eastern China and Mexico are higher than over South Africa. The OMPS data show slightly higher SO₂ loading over eastern China and lower SO₂ loading over Mexico and South



Africa as compared with OMI products. The annual regional averaged SO₂ columns over Eastern China are 0.79 and 0.69 DUs for OMPS and OMI, respectively. On an annual basis the spatial correlation between the two instruments is high (>0.9). Particularly over Mexico, the spatial patterns of high SO₂ (> ~1 DU) from OMPS and OMI are similar. Regional annual average SO₂ loading is 0.58 DU and 0.51 DU for OMPS and OMI, respectively, and the spatial correlation coefficient is 0.94. South Africa shows smallest SO₂ loading and the best overall agreement between OMI and OMPS as compared with the other two regions. Regional annual average SO₂ loading from OMPS is 0.29 DU and from OMI is 0.28 DU. The spatial correlation coefficient in SO₂ loading from the two instruments in this region is 0.95. Three distinct “hot” spots (SO₂ loading > 0.53 DU) are captured by both OMPS and OMI in South Africa. These correspond to clusters of coal-fired power plants also detected in OMI NO₂ data (Duncan et al., 2016). We find that peak SO₂ columns from OMPS are smaller than from OMI, possibly due to the lower OMPS spatial resolution. This is less of an issue for eastern China and Mexico, where the regional loading of SO₂ pollution is much higher and more homogeneous due to the numerous sources.

The differences in the spatial distributions of annual mean SO₂ between OMPS and OMI over these regions in 2012 are also presented in Figure 2 (bottom row). Larger differences between the two instruments are found in areas with the strongest SO₂ sources. The maximum SO₂ differences between OMPS and OMI are 0.64 DU (29%), -2.0 (-61%) DU, and -0.54 (-41%) DU over eastern China, Mexico, and South Africa, respectively. For eastern China, the SO₂ loading is relatively high for the entire region due to the large cluster of point and area sources. The higher loading in OMPS retrievals may be due to the minor difference in algorithm implementation (see Section 2.2) and the different sampling between the two instruments. As for Mexico and South Africa, the SO₂ sources (and distributions) are more local. The negative bias of OMPS as compared with OMI may reflect the different spatial resolutions between the two instruments and their different capabilities of resolving point sources. In addition, the retrievals over Mexico are strongly affected by emissions from the Popocatepetl volcano (elevation 5426 m) and likely biased high since the volcanic plume is elevated while our retrievals assume a boundary layer profile. As a result, the difference between the two instruments may be exacerbated. The difference is the largest for 2012, when Popocatepetl was most active with approximately two times the emissions of 2013 and 2014 (Fioletov et al., 2016). For these two latter years, the OMPS-OMI maximum differences are -0.69 and -0.68, respectively. Another factor that may cause the relatively large differences over Mexico is that the elevated volcanic plume may be transported relatively quickly; the difference in sampling time between OMI and OMPS may cause relatively large differences in the spatial distributions.

Table 1 presents annual average SO₂ loading for each region and the spatial correlation between OMI and OMPS for each year between 2012 and 2015. Over eastern China average SO₂ loading decreased significantly in 2015 (~0.37 DU from OMI) as compared with 2012 (~0.69 DU from OMI), in agreement with (Krotkov et al., 2016). We note that the spatial correlation between OMI and OMPS also decreases with reduction in average SO₂ loading, possibly due to reduction of the SO₂ variability.



3.2 Regional daily SO₂

In this section we compare regional SO₂ mass on a daily basis derived from the two instruments. Daily regional SO₂ masses are calculated as a sum of the SO₂ mass from the grid cells (0.5°X0.5°) that satisfy our filtering criteria (see section 2.3). We only consider grid cells that have valid SO₂ retrievals from both instruments. This ensures consistent spatial
5 sampling between the two instruments. We consider days only with the number of non-empty grid cells > 25% of total grids cells in each region for both OMI and OMPS, and temporal correlations (R) between OMI and OMPS in Table 2 are calculated based on daily SO₂ masses from two instruments and satisfied above criteria. In Table 2, we show results of linear regression analysis using reduced major axis fitting that accounts for the uncertainties in both OMI and OMPS data. Results of the ordinary least squares linear regression analysis are also provided in Table 2.

10 Figure 3 compares OMPS and OMI daily regional SO₂ masses over the eastern China domain from 2012 to 2015. The year 2013 has the best sampling (more than 200 days) and the best temporal correlation between the instruments (r=0.88 and the regression slope is 0.98). The other three years, despite reduced sampling, also have good temporal correlations (r = 0.79-0.86) and linear regression slopes close to unity (0.86 to 0.98). Eastern China area is located in the mid-latitudes. In the cold season, frequent cold-front passages may bring air mass with large O₃, a major interfering species
15 in SO₂ retrievals. This, together with higher solar zenith angles, and possible snow events, leads to relatively large noise and potential biases in retrieved SO₂ in winter months. When we restrict our analysis to the warm season (Apr.-Oct.), the temporal correlation and regression slope between the two instruments improves (r = 0.82-0.87 and slope is 0.92-1.01 (Table 3)). Although the SO₂ columns over the region remain the world's highest, the decreasing trend is also significant. Annual averaged OMI SO₂ masses in this region were 8.4, 8.8, 6.2, and 4.1 kt (Table 4) in 2012, 2013, 2014, and 2015, respectively.
20 This is in line with a ~50% decrease over the North China Plain region also derived from OMI and OMPS (Krotkov et al., 2016). Overall, OMPS SO₂ masses are slightly higher as compared with OMI. The temporal correlation between OMI and OMPS reduces from r=0.85-0.88 in 2012-13 to r~0.79 in 2014-15, which may be explained by reduced SO₂ emissions and pollution levels.

The Mexico region is located in the tropics where the SO₂ retrievals from PCA algorithm are less influenced by
25 weather patterns and the total O₃ columns are less variable as compared with middle and high latitude regions. Due to the high frequency of cloud occurrence in this region, the number of days with valid SO₂ retrievals for each year is less than that from eastern China. Figure 4 shows that OMI and OMPS retrieved consistent SO₂ masses in all four years. The temporal correlation between the instruments is also the highest (r=0.91-0.96) and regression line slopes are 0.91-0.99, which indicates that OMPS shows a relatively small multiplicative low bias as compared with OMI.

30 Compared to eastern China and Mexico, averaged SO₂ masses in South Africa are much smaller. The average SO₂ spatial distribution shows hot spots around major point source areas and less widespread than in the other two regions. The maximum SO₂ mass is less than 20 kt in 2012-2014 as shown in Figure 5. The SO₂ mass exceeding 30 kt in April-May 2015



resulted from the passage of a volcanic SO₂ plume from the April 2015 Calbuco eruption in Chile http://so2.gsfc.nasa.gov/pix/special/2015/calbuco/Calbuco_20150427_omiomps_1.html

After removing those days, the linear regression slope increased from 0.76 to 0.83. The 2015 averaged SO₂ mass in the South Africa region decreases from 4.6 kt to 3.6 kt for OMPS, and from 4.3 kt to 3.4 kt for OMI, which are comparable to
5 SO₂ masses in other years (Table 4). Overall, SO₂ masses in the South Africa region from the two instruments are in a good agreement.

We also investigated the correlation between the spatial distributions of the OMI and OMPS PCA retrievals on a daily basis as shown in Figure 6. We excluded SO₂ mass < 2.5 kt over the area since for those clean days, OMI and OMPS retrievals are near their noise level. Mexico shows the best correlation among the three regions; 82% of the days have spatial
10 correlation coefficient $r > 0.6$. The other two regions also have more than half of all qualified days showing daily spatial correlation coefficients $r > 0.6$. These comparisons over three regions suggest that the daily spatial distributions of SO₂ from OMI and OMPS PCA retrievals are correlated for even moderately polluted days.

3.3 Instrument performance and trends

Instrument degradation may affect SO₂ retrievals. We examined the trends in spatial standard deviation (STD) and
15 standard errors (STE = divided by the square root of the number of daily observations) of the daily SO₂ noise over three clean regions in Pacific (150°W-120°W). Figure 7 shows median, and 25th and 75th percentiles of daily SO₂ STD and STE in August in each year in Fig. 7. Except tropical Pacific region with latitudes between 10°S and 10°N, we selected the latitudes as the same as those of our eastern China and South Africa regions (called north and south Pacific regions, respectively) and similar filtering has been applied to the data. Over these background regions, the SO₂ levels are below satellite detection
20 limits and as expected, the medians of daily averaged SO₂ columns were statistically equal to zero for the regions (-0.06-0.04 DU for OMI and 0.07-0.1 DU for OMPS). The OMI STDs increased by ~10% from 2005 to 2015 over the north Pacific and tropical Pacific regions, which can be explained by increasing CCD detector noise after 12 years of continuous operation in space. As expected the OMPS STDs do not show significant changes during its first 4 years in space. We note that OMPS STDs (medians ~0.3DU) are roughly half the OMI values (medians ~0.5-0.7DU), which could be explained by the larger
25 OMPS FOV, higher signal-to-noise, and OMI long-term degradation. We note that the OMI STEs in 2005 are actually smaller than OMPS in 2012, which may be explained by higher OMI spatial resolution and a resulting larger number of measurements over the same region. However, the OMI STEs increased after 2008 owing to the row anomaly that decreased the number of available observations and became comparable to the OMPS STEs in recent years.

4 Conclusions

30 Taking advantage of the 4-year overlap between OMI and OMPS local afternoon measurements and applying the same PCA algorithm to retrieve SO₂, we demonstrated that OMI and OMPS SO₂ retrievals are highly consistent for the world's most



polluted regions from 2012 through 2015. The annually averaged spatial correlation coefficient of SO₂ loading over eastern China, Mexico, and South Africa between OMI and OMPS are greater than ~0.9 in each year. The daily SO₂ temporal correlation coefficients are 0.86, 0.95, and 0.91 for eastern China, Mexico, and South Africa, respectively. The difference of regional averaged SO₂ mass is less than 10% between the two instruments for the three regions in each year except over
5 Mexico in 2013, which difference is 14%. Good consistency between the two instruments provides confidence that the OMPS nadir mapper currently flying onboard SNPP satellite and similar future instruments planned for the follow-up JPSS-1,-2,-3,-4 NOAA operational satellites, which will have spatial resolution similar to OMI, can be used to continue long-term OMI SO₂ record started in 2004.

Data availability

- 10 The OMI PBL SO₂ product (OMSO2 v1.2.0) is publicly available from the NASA Goddard Earth Sciences (GES) Data and Information Services Center (DISC) (http://disc.sci.gsfc.nasa.gov/Aura/data-holdings/OMI/omso2_v003.shtml).
OMPS PBL monthly SO₂ product is publicly available from Aura Validation Data Center (AVDC) (<http://avdc.gsfc.nasa.gov/index.php?site=1868800100>)

Acknowledgement

- 15 The authors acknowledge the NASA Earth Science Division (ESD) Aura Science Team program for funding of OMI product development and analysis. The Dutch and Finnish built OMI instrument is part of the NASA's Earth Observing System (EOS) Aura satellite payload. The OMI project is managed by the Royal Meteorological Institute of the Netherlands (KNMI) and the Netherlands Space Agency (NSO). CL acknowledges partial support from NASA's Earth Science New Investigator program in developing the OMPS SO₂ algorithm (Grant #: NNX14A102G).
- 20 The authors would like to thank the NASA OMPS ozone Product Evaluation and Test Element (PEATE) team for updating the OMPS calibration and producing the OMPS Level 1b data used in this analysis. We thank the OMI calibration team, led by KNMI, for the calibrated OMI level 1b data used here and the OMI Science Investigator-led Processing System (SIPS) team for processing the OMI data.

References

- 25 Carn, S. A., Krueger, A. J., Krotkov, N. A., Yang, K. and Levelt, P. F.: Sulfur dioxide emissions from Peruvian copper smelters detected by the Ozone Monitoring Instrument, *Geophys. Res. Lett.*, 34(9), L09801, doi:10.1029/2006GL029020, 2007.
- Dittman, M. G., Ramberg, E., Chrisp, M., Rodriguez, J. V., Sparks, A. L., Zaun, N. H., Hendershot, P., Dixon, T., Philbrick,



- R. H. and Wasinger, D.: Nadir ultraviolet imaging spectrometer for the NPOESS Ozone Mapping and Profiler Suite (OMPS), in Earth Observing Systems VII, Proceedings of SPIE vol.4814, edited by W. L. Barnes, pp. 111–119, International Society for Optics and Photonics., 2002.
- Duncan, B. N., Lamsal, L. N., Thompson, A. M., Yoshida, Y., Lu, Z., Streets, D. G., Hurwitz, M. M. and Pickering, K. E.: A
5 space-based, high-resolution view of notable changes in urban NO_x pollution around the world (2005-2014), *J. Geophys. Res. Atmos.*, 121(2), 976–996, doi:10.1002/2015JD024121, 2016.
- Eisinger, M. and Burrows, J. P.: Tropospheric sulfur dioxide observed by the ERS-2 GOME instrument, *Geophys. Res. Lett.*, 25(22), 4177–4180, doi:10.1029/1998GL900128, 1998.
- Faloona, I., Conley, S. A., Blomquist, B., Clarke, A. D., Kapustin, V., Howell, S., Lenschow, D. H. and Bandy, A. R.: Sulfur
10 dioxide in the tropical marine boundary layer: dry deposition and heterogeneous oxidation observed during the Pacific Atmospheric Sulfur Experiment, *J. Atmos. Chem.*, 63(1), 13–32, doi:10.1007/s10874-010-9155-0, 2010.
- Fioletov, V. E., McLinden, C. a., Krotkov, N., Yang, K., Loyola, D. G., Valks, P., Theys, N., Van Roozendaal, M., Nowlan, C. R., Chance, K., Liu, X., Lee, C. and Martin, R. V.: Application of OMI, SCIAMACHY, and GOME-2 satellite SO₂ retrievals for detection of large emission sources, *J. Geophys. Res. Atmos.*, 118(19), 11399–11418, doi:10.1002/jgrd.50826,
15 2013.
- Fioletov, V. E., McLinden, C. A., Krotkov, N. and Li, C.: Lifetimes and emissions of SO₂ from point sources estimated from OMI, *Geophys. Res. Lett.*, 42(6), 1969–1976, doi:10.1002/2015GL063148, 2015.
- Fioletov, V. E., McLinden, C. A., Krotkov, N., Li, C., Joiner, J., Theys, N., Carn, S., and Moran, M. D.: A global catalogue of large SO₂ sources and emissions derived from the Ozone Monitoring Instrument, *Atmos. Chem. Phys.*, 16, 11497–11519,
20 doi:10.5194/acp-16-11497-2016, 2016.
- Flynn, L., Long, C., Wu, X., Evans, R., Beck, C. T., Petropavlovskikh, I., McConville, G., Yu, W., Zhang, Z., Niu, J., Beach, E., Hao, Y., Pan, C., Sen, B., Novicki, M., Zhou, S. and Seftor, C.: Performance of the Ozone Mapping and Profiler Suite (OMPS) products, *J. Geophys. Res. Atmos.*, 119(10), 6181–6195, doi:10.1002/2013JD020467, 2014.
- de Foy, B., Krotkov, N. A., Bei, N., Herndon, S. C., Huey, L. G., Martínez, A.-P., Ruiz-Suárez, L. G., Wood, E. C., Zavala,
25 M. and Molina, L. T.: Hit from both sides: tracking industrial and volcanic plumes in Mexico City with surface measurements and OMI SO₂ retrievals during the MILAGRO field campaign, *Atmos. Chem. Phys.*, 9(24), 9599–9617, doi:10.5194/acp-9-9599-2009, 2009.
- Klimont, Z., Smith, S. J. and Cofala, J.: The last decade of global anthropogenic sulfur dioxide: 2000–2011 emissions, *Environ. Res. Lett.*, 8(1), 014003, doi:10.1088/1748-9326/8/1/014003, 2013.
- 30 Krotkov, N. A., Cam, S. A., Krueger, A. J., Bhartia, P. K. and Yang, K.: Band residual difference algorithm for retrieval of SO₂ from the Aura Ozone Monitoring Instrument (OMI), *IEEE Trans. Geosci. Remote Sens.*, 44(5), 1259–1266, doi:10.1109/TGRS.2005.861932, 2006.
- Krotkov, N. A., McClure, B., Dickerson, R. R., Carn, S. A., Li, C., Bhartia, P. K., Yang, K., Krueger, A. J., Li, Z., Levelt, P. F., Chen, H., Wang, P. and Lu, D.: Validation of SO₂ retrievals from the Ozone Monitoring Instrument over NE China, *J.*



- Geophys. Res. Atmos., 113(16), doi:10.1029/2007JD008818, 2008.
- Krotkov, N. A., Schoeberl, M. R., Morris, G. A., Carn, S. and Yang, K.: Dispersion and lifetime of the SO₂ cloud from the August 2008 Kasatochi eruption, *J. Geophys. Res.*, 115(D2), D00L20, doi:10.1029/2010JD013984, 2010.
- Krotkov, N. A., McLinden, C. A., Li, C., Lamsal, L. N., Celarier, E. A., Marchenko, S. V., Swartz, W. H., Bucsela, E. J.,
 5 Joiner, J., Duncan, B. N., Boersma, K. F., Veefkind, J. P., Levelt, P. F., Fioletov, V. E., Dickerson, R. R., He, H., Lu, Z. and Streets, D. G.: Aura OMI observations of regional SO₂ and NO₂ pollution changes from 2005 to 2015, *Atmos. Chem. Phys.*, 16(7), 4605–4629, doi:10.5194/acp-16-4605-2016, 2016.
- Krueger, A. J.: Sighting of el chichon sulfur dioxide clouds with the nimbus 7 total ozone mapping spectrometer., *Science*, 220(4604), 1377–9, doi:10.1126/science.220.4604.1377, 1983.
- 10 Lee, C., Martin, R. V., Van Donkelaar, A., O’Byrne, G., Krotkov, N., Richter, A., Huey, L. G. and Holloway, J. S.: Retrieval of vertical columns of sulfur dioxide from SCIAMACHY and OMI: Air mass factor algorithm development, validation, and error analysis, *J. Geophys. Res. Atmos.*, 114(22), D22303, doi:10.1029/2009JD012123, 2009.
- Levelt, P. F., Hilsenrath, E., Leppelmeier, G. W., Oord, G. H. J. Van Den, Bhartia, P. K., Tamminen, J., Haan, J. F. De and Veefkind, J. P.: Science Objectives of the Ozone Monitoring Instrument, , 44(5), 1199–1208, 2006a.
- 15 Levelt, P. F., Oord, G. H. J. Van Den, Dobber, M. R., Mälkki, A., Visser, H., Vries, J. De, Stammes, P., Lundell, J. O. V and Saari, H.: The Ozone Monitoring Instrument, *IEEE Trans. Geosci. Remote Sens.*, 44(5), 1093–1101, 2006b.
- Li, C., Krotkov, N. A., Dickerson, R. R., Li, Z., Yang, K., and Chin, M.: Transport and evolution of a pollution plume from northern China: A satellite-based case study, *J. Geophys. Res.*, 115, D00K03, doi:10.1029/2009JD012245, 2010a.
- Li, C., Zhang, Q., Krotkov, N. A., Streets, D. G., He, K., Tsay, S.-C., and Gleason, J. F.: Recent large reduction in sulfur
 20 dioxide emissions from Chinese power plants observed by the Ozone Monitoring Instrument, *Geophys. Res. Lett.*, 37, L08807, doi:10.1029/2010GL042594, 2010b.
- Li, C., Joiner, J., Krotkov, N. a. and Bhartia, P. K.: A fast and sensitive new satellite SO₂ retrieval algorithm based on principal component analysis: Application to the ozone monitoring instrument, *Geophys. Res. Lett.*, 40(23), 6314–6318, doi:10.1002/2013GL058134, 2013.
- 25 Li., C, Krotkov, N. A., Carn, S., Zhang, Y., Spurr, R. J. D., and Joiner, J.: New-generation NASA Aura Ozone Monitoring Instrument volcanic SO₂ dataset: Algorithm description, initial results, and continuation with the Suomi-NPP Ozone Mapping and Profiler Suite, *Atmos. Meas. Tech.*, submitted, 2016.
- McLinden, C. A., Fioletov, V., Boersma, K. F., Kharol, S. K., Krotkov, N., Lamsal, L., Makar, P. A., Martin, R. V., Veefkind, J. P. and Yang, K.: Improved satellite retrievals of NO₂ and SO₂ over the Canadian oil sands and comparisons
 30 with surface measurements, *Atmos. Chem. Phys.*, 14(7), 3637–3656, doi:10.5194/acp-14-3637-2014, 2014.
- McLinden, C. A., Fioletov, V., Krotkov, N. A., Li, C., Boersma, K. F. and Adams, C.: A Decade of Change in NO₂ and SO₂ over the Canadian Oil Sands As Seen from Space., *Environ. Sci. Technol.*, 50(1), 331–7, doi:10.1021/acs.est.5b04985, 2016a.
- McLinden, C. A., Fioletov, V., Shephard, M. W., Krotkov, N., Li, C., Martin, R. V., Moran, M. D. and Joiner, J.: Space-



- based detection of missing sulfur dioxide sources of global air pollution, *Nat. Geosci.*, (May), 1–7, doi:10.1038/ngeo2724, 2016b.
- Nowlan, C. R., Liu, X., Chance, K., Cai, Z., Kurosu, T. P., Lee, C. and Martin, R. V.: Retrievals of sulfur dioxide from the Global Ozone Monitoring Experiment 2 (GOME-2) using an optimal estimation approach: Algorithm and initial validation, *J. Geophys. Res.*, 116(D18), D18301, doi:10.1029/2011JD015808, 2011.
- Schoeberl, M. R., Douglass, A. R., Hilsenrath, E., Bhartia, P. K., Beer, R., Waters, J. W., Gunson, M. R., Froidevaux, L., Gille, J. C., Barnett, J. J., Levelt, P. F. and DeCola, P.: Overview of the EOS aura mission, *IEEE Trans. Geosci. Remote Sens.*, 44(5), 1066–1072, doi:10.1109/TGRS.2005.861950, 2006.
- Seftor, C. J., Jaross, G., Kowitt, M., Haken, M., Li, J. and Flynn, L. E.: Postlaunch performance of the Suomi National Polar-orbiting Partnership Ozone Mapping and Profiler Suite (OMPS) nadir sensors, *J. Geophys. Res. Atmos.*, 119(7), 4413–4428, doi:10.1002/2013JD020472, 2014.
- Smith, S. J., van Aardenne, J., Klimont, Z., Andres, R. J., Volke, A. and Delgado Arias, S.: Anthropogenic sulfur dioxide emissions: 1850–2005, *Atmos. Chem. Phys.*, 11(3), 1101–1116, doi:10.5194/acp-11-1101-2011, 2011.
- Streets, D. G., Canty, T., Carmichael, G. R., de Foy, B., Dickerson, R. R., Duncan, B. N., Edwards, D. P., Haynes, J. A., Henze, D. K., Houyoux, M. R., Jacob, D. J., Krotkov, N. A., Lamsal, L. N., Liu, Y., Lu, Z., Martin, R. V., Pfister, G. G., Pinder, R. W., Salawitch, R. J. and Wecht, K. J.: Emissions estimation from satellite retrievals: A review of current capability, *Atmos. Environ.*, 77, 1011–1042, doi:10.1016/j.atmosenv.2013.05.051, 2013.
- Yang, K., Dickerson, R. R., Carn, S. A., Ge, C. and Wang, J.: First observations of SO₂ from the satellite Suomi NPP OMPS: Widespread air pollution events over China, *Geophys. Res. Lett.*, 40(18), 4957–4962, doi:10.1002/grl.50952, 2013.



Tables

Table 1. The averaged SO₂ loading (unit: DU) in 2012-2015 from OMI and OMPS and their spatial correlations for three regions: eastern China, Mexico, and South Africa.

	Eastern China				Mexico				South Africa			
	2012	2013	2014	2015	2012	2013	2014	2015	2012	2013	2014	2015
OMI	0.69	0.61	0.50	0.37	0.51	0.42	0.32	0.42	0.28	0.28	0.27	0.38
OMPS	0.79	0.67	0.52	0.36	0.58	0.45	0.34	0.41	0.29	0.29	0.28	0.35
R	0.96	0.96	0.95	0.92	0.94	0.97	0.95	0.94	0.95	0.96	0.97	0.95

5

Table 2. The total number of days with valid SO₂ for both OMI and OMPS for each year. Number of samples within $\pm 50\%$ and $\pm 75\%$ agreement, temporal correlation coefficient (R), and the slopes and intercepts from reduced major axis fitting and ordinary least square fitting for each year and all years.

10

	Eastern China	Mexico	South Africa	
2012	Total days:	143	141	163
	Reduced Major Axis:	$Y = 0.97X + 0.75$	$Y = 0.99X + 0.41$	$Y = 0.96X + 0.32$
	Ordinary least square:	$Y = 0.83X + 2.56$	$Y = 0.95X + 0.72$	$Y = 0.86X + 0.78$
	Within +- 50%:	129	121	145
	Within +- 75%:	75	88	96
	R	0.85	0.96	0.90
2013	Total days:	213	144	193
	Reduced Major Axis:	$Y = 0.98X + 0.93$	$Y = 0.99X + 0.86$	$Y = 0.96X + 0.25$
	Ordinary least square:	$Y = 0.86X + 2.27$	$Y = 0.94X + 1.18$	$Y = 0.81X + 0.93$
	Within +- 50%:	189	120	168
	Within +- 75%:	109	79	108
	R	0.88	0.96	0.84
2014	Total days:	159	133	186
	Reduced Major Axis:	$Y = 0.86X + 1.40$	$Y = 0.91X + 0.65$	$Y = 0.89X + 0.28$
	Ordinary least square:	$Y = 0.68X + 3.00$	$Y = 0.83X + 1.05$	$Y = 0.78X + 0.77$



	Within +- 50%:	134	109	164
	Within +- 75%:	71	66	101
	R	0.79	0.91	0.88
	Total days:	142	126	199
	Reduced Major Axis:	$Y = 0.91X + 0.41$	$Y = 0.95X + 0.68$	$Y = 0.76X + 0.93$
	Ordinary least square:	$Y = 0.72X + 1.64$	$Y = 0.89X + 1.05$	$Y = 0.71X + 1.22$
2015	Within +- 50%:	120	106	181
	Within +- 75%:	78	75	116
	R	0.79	0.94	0.94
	Total days:	657	544	741
	Reduced Major Axis:	$Y = 0.96X + 0.68$	$Y = 0.97X + 0.60$	$Y = 0.80X + 0.82$
	Ordinary least square:	$Y = 0.82X + 2.04$	$Y = 0.92X + 0.93$	$Y = 0.73X + 1.16$
2012~ 2015	Within +- 50%:	572	456	658
	Within +- 75%:	333	308	421
	R	0.86	0.95	0.91



Table 3. Same as Table 2, but for the warm season (Apr.-Oct.) over eastern China.

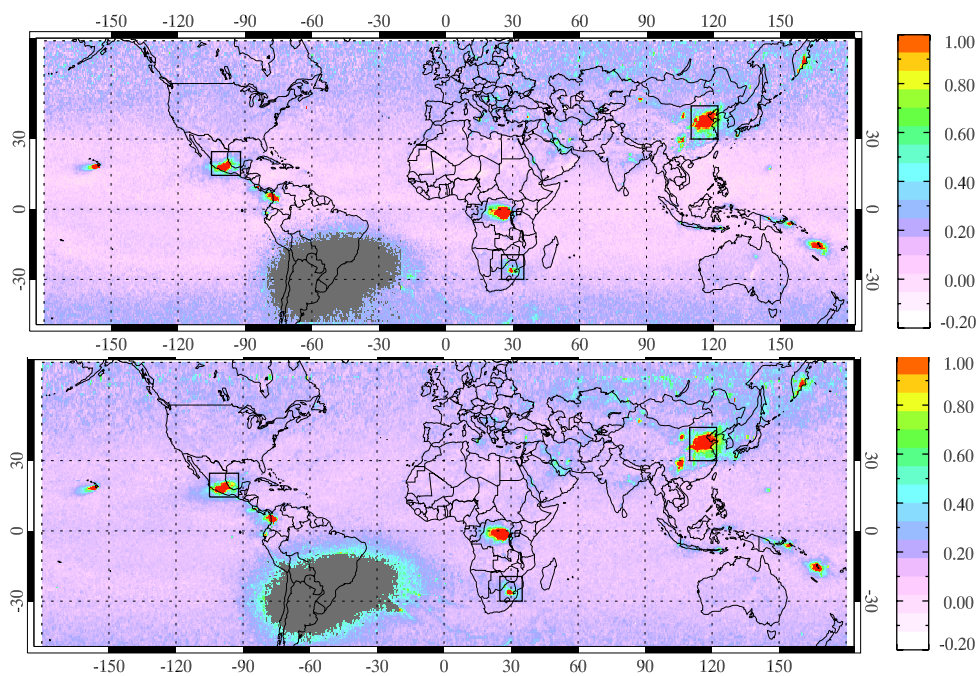
2012	Total days:	105
	Reduced Major Axis:	$Y = 0.92X + 1.00$
	Ordinary least square:	$Y = 0.80X + 2.21$
	R	0.87
2013	Total days:	132
	Reduced Major Axis:	$Y = 0.95X + 1.62$
	Ordinary least square:	$Y = 0.83X + 2.67$
	R	0.87
2014	Total days:	101
	Reduced Major Axis:	$Y = 0.98X + 1.12$
	Ordinary least square:	$Y = 0.83X + 2.09$
	R	0.85
2015	Total days:	96
	Reduced Major Axis:	$Y = 1.01X + 0.46$
	Ordinary least square:	$Y = 0.83X + 1.34$
	R	0.82

Table 4. Averaged SO₂ mass (unit: kt) over eastern China, Mexico, and South Africa in 2012, 2013, 2014, and 2015 for both
 5 OMI and OMPS.

		2012	2013	2014	2015
Eastern China	OMI	8.4	8.8	6.2	4.1
	OMPS	9.1	9.8	6.4	4.0
Mexico	OMI	5.9	4.2	3.2	4.0
	OMPS	6.3	4.9	3.4	4.4
South Africa	OMI	3.3	3.3	3.2	4.6
	OMPS	3.4	3.3	3.1	4.3



Figures



5 **Figure 1: Annual SO₂ loading (unit: DU) in 2012 for OMI (top) and OMPS (bottom). Both OMI and OMPS SO₂ maps are bias adjusted (monthly based) and gridded to 0.5°X0.5° grid cells. The three black boxes are regions for eastern China, Mexico, and South Africa, respectively, that will be examined in more detail below. The grey shaded area shows the area affected by the South America Anomaly.**

10

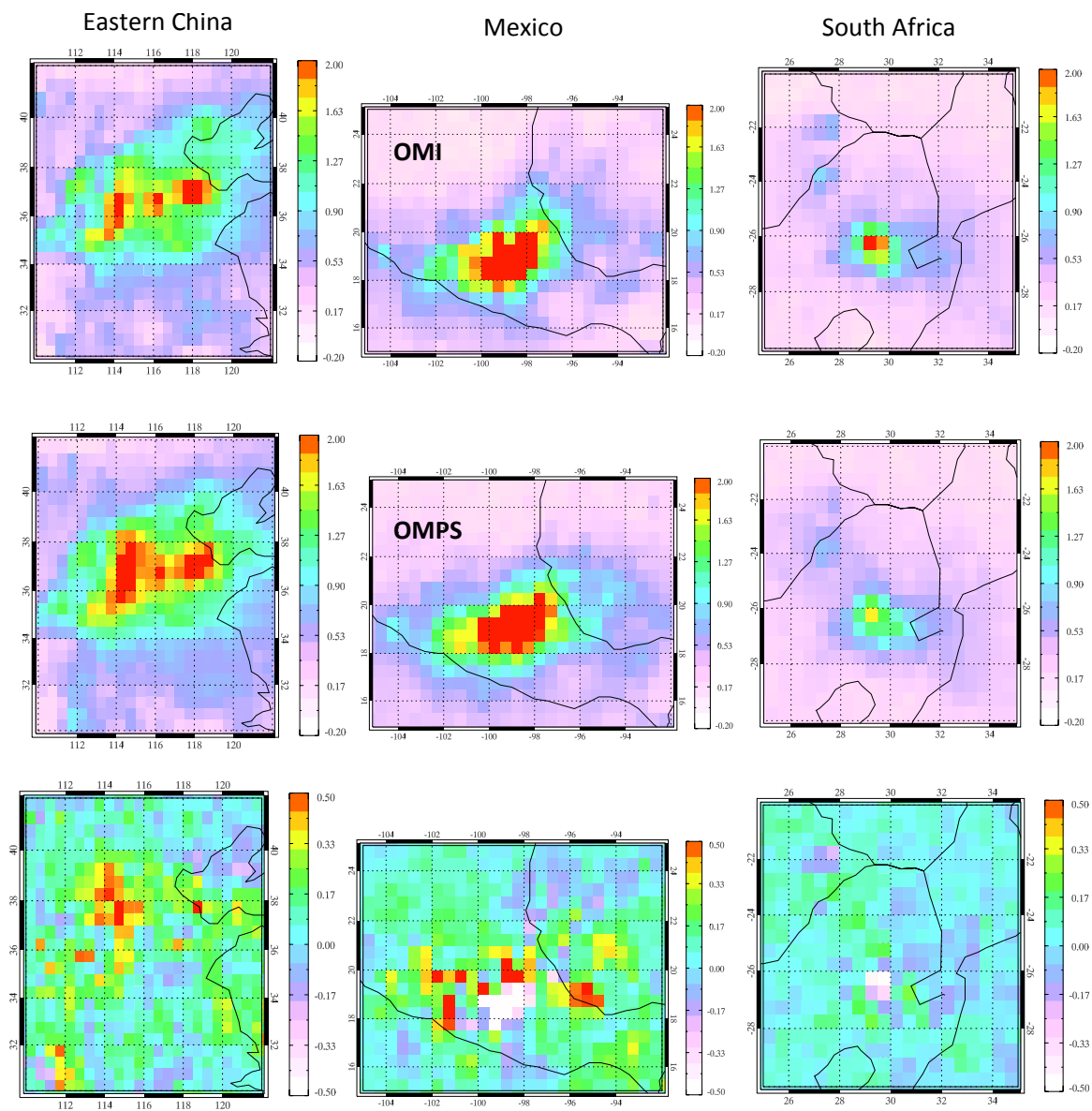


Figure 2: Annual SO₂ loading (unit: DU) over eastern China (left), Mexico (middle), and South Africa (right) for OMI (top), OMPS (center), and differences between OMPS and OMI (bottom) in 2012. SO₂ columns amounts are gridded to 0.5°X0.5° grid cells.

5

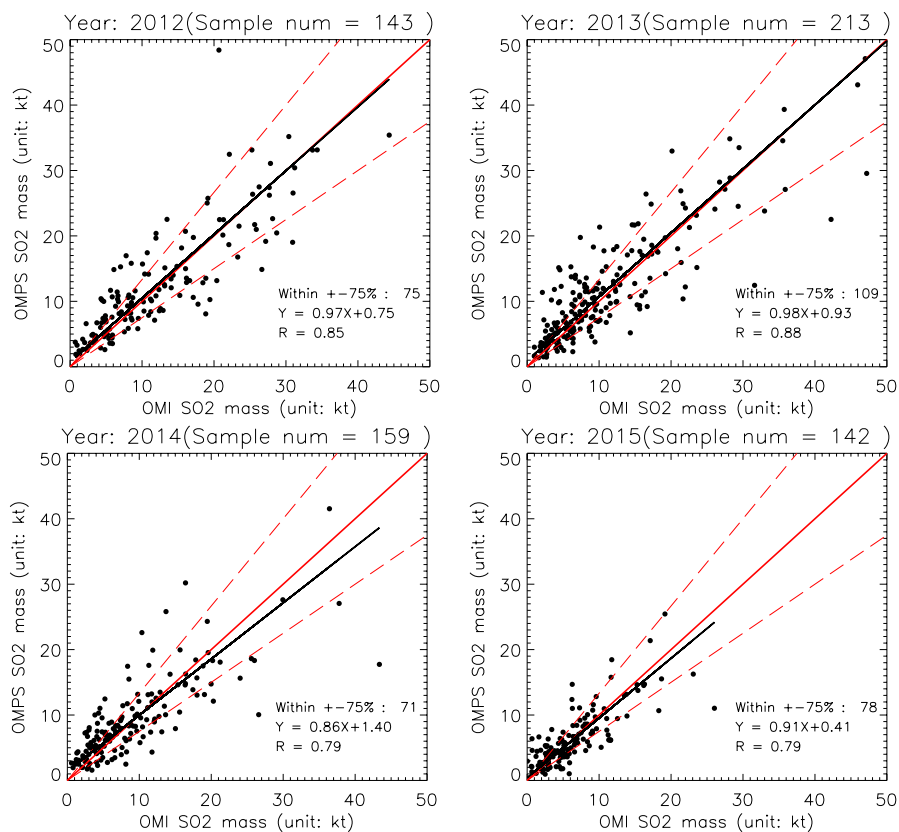


Figure 3: Eastern China regional-daily SO₂ mass (unit: kt) compared between OMI and OMPS for years 2012, 2013, 2014, and 2015. Red solid line is the 1:1 line and dashed lines are +/-75%. Black line is reduced major axis fitting from OMI and OMPS SO₂ mass. R is the temporal correlation coefficient. The number of samples within +/-75% is also presented here.

5

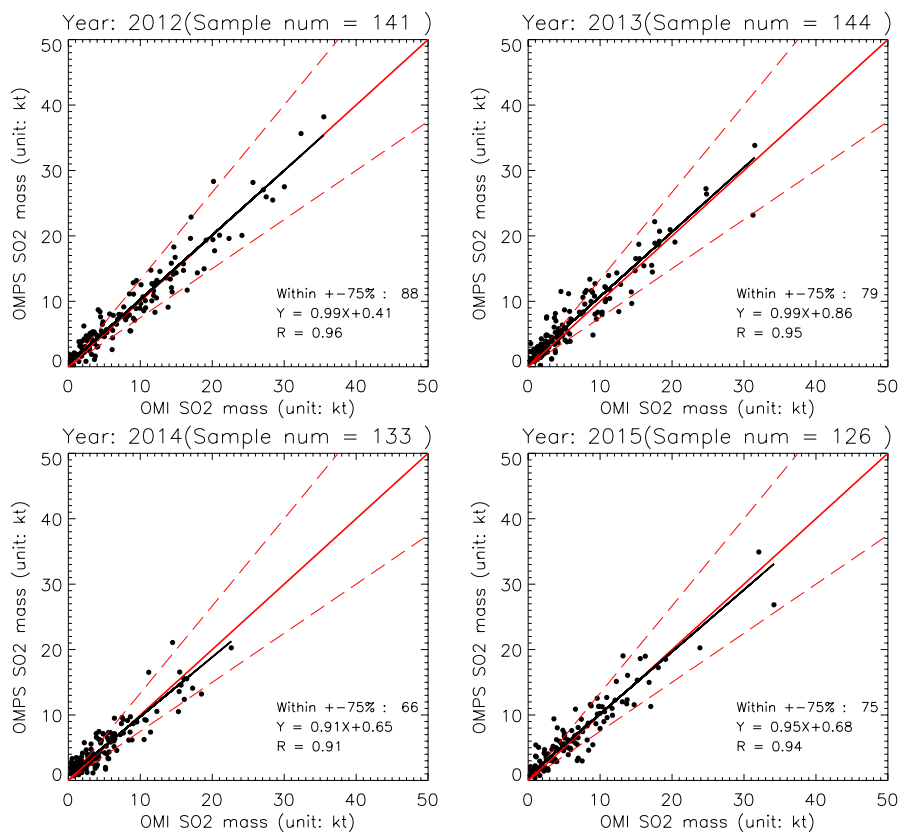


Figure 4: Same as Figure 3, but for the Mexico region.

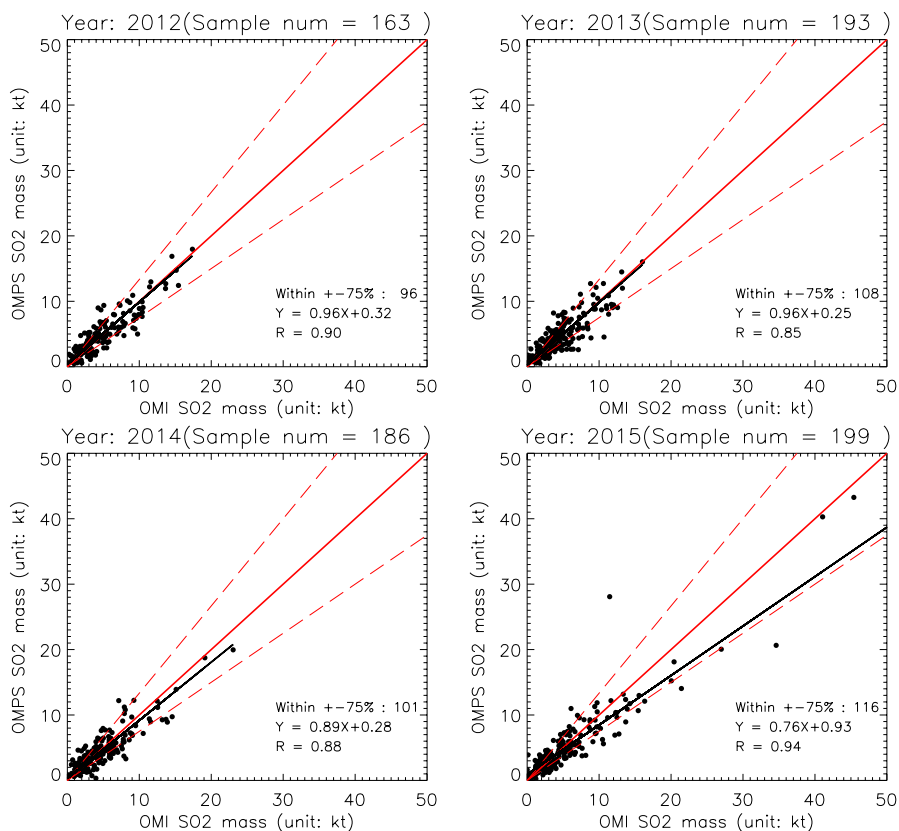


Figure 5: Same as Figure 3, but for the South Africa.

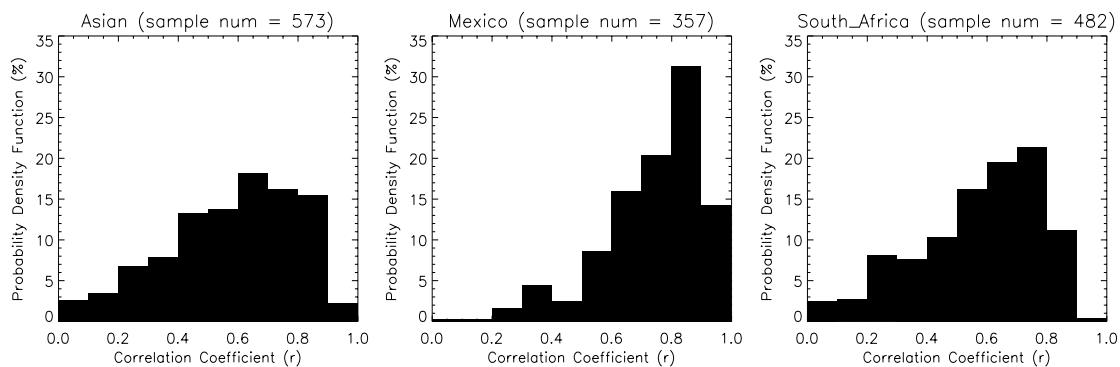
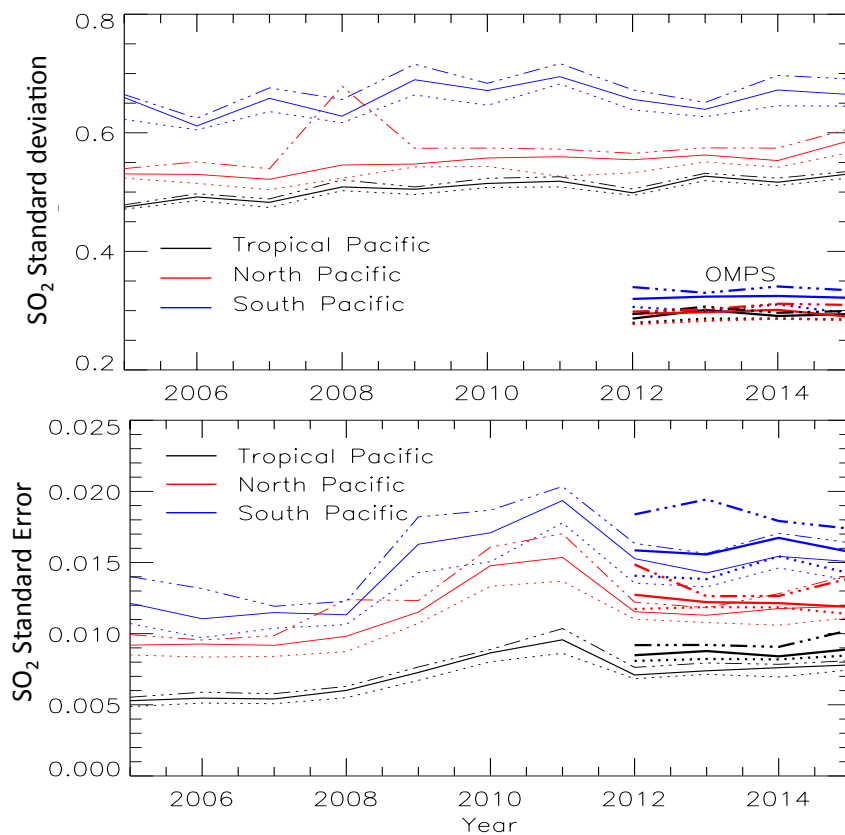


Figure 6: Probability distribution functions (PDFs) of daily spatial correlations over eastern China (left), Mexico (center), and South Africa (right) from 2012 to 2015.

5



5 **Figure 7: Standard deviation (STD, top) and Standard Error (STE, bottom) of SO₂ noise (DU) averaged over clean background regions in the north Pacific (150W-120W), between 30°N-42°N (Red), in tropical Pacific between 10°S-10°N (black), and south Pacific between 30°S-20°S (blue) Pacific regions in August of each year from 2005 to 2015. Solid lines are medians of daily SO₂ STD from each month (31 days), and dashed lines are 25% and 75% of daily SO₂ STD from each month, respectively. OMI data start in 2005 and OMPS data start in 2012. The OMI STD peak in 2008 over North Pacific results from the Okmok and Kasatochi eruptions [Krotkov et al., 2010].**